remote sensing

MDPI

Article

RETRACTED: An Infrared Small Target Detection Method Based on a Weighted Human Visual Comparison Mechanism for Safety Monitoring

Yuanyuan Chen [1,2], Huiqian Wang [3,*], Yu Pang [3], Jinhui Han [2], En Mou [1,4] and Enling Cao [5]

[1] School of Communication and Information Engineering, Chongqing University of Posts and Telecommunication, Chongqing 400065, China; chenyuanyuan@zknu.edu.cn (Y.C.)
[2] College of Physics and Telecommunication Engineering, Zhoukou Normal University, Zhoukou 466001, China
[3] School of Optoelectronic Engineering, Chongqing University of Posts and Telecommunication, Chongqing 400065, China
[4] School of Medical Information and Engineering, Southwest Medical University, Luzhou 646000, China
[5] School of Software Engineering, Chongqing University of Posts and Telecommunications, Chongqing 400065, China
* Correspondence: wanghq@cqupt.edu.cn

Abstract: Infrared small target detection is a crucial technology in both military and civilian applications, including surveillance, security, defense, and combat. However, accurate infrared detection of small targets in real-time is challenging due to their small size and similarity in gray level and texture with the surrounding environment, as well as interference from the infrared imaging systems in unmanned aerial vehicles (UAVs). This article proposes a weighted local contrast method based on the contrast mechanism of the human visual system. Initially, a combined contrast ratio is defined that stems from the pixel-level divergence between the target and its neighboring pixels. Then, an improved regional intensity level is used to establish a weight function with the concept of ratio difference combination, which can effectively suppress complex backgrounds and random noise. In the final step, the contrast and weight functions are combined to create the final weighted local contrast method (WRDLCM). This method does not require any preconditioning and can enhance the target while suppressing background interference. Additionally, it is capable of detecting small targets even when their scale changes. In the experimental section, our algorithm was compared with some popular methods, and the experimental findings indicated that our method showed strong detection capability based on the commonly used performance indicators of the ROC curve, SCRG, and BSF, especially in low signal-to-noise ratio situations. In addition, unlike deep learning, this method is appropriate for small sample sizes and is easy to implement on FPGA hardware.

Keywords: IR small target; human visual system; local contrast; improved regional intensity level (IRIL)

check for updates

Citation: Chen, Y.; Wang, H.; Pang, Y.; Han, J.; Mou, E.; Cao, E. RETRACTED: An Infrared Small Target Detection Method Based on a Weighted Human Visual Comparison Mechanism for Safety Monitoring. *Remote Sens.* **2023**, *15*, 2922. https://doi.org/10.3390/rs15112922

Academic Editors: Riccardo Roncella and Pedro Melo-Pinto

Received: 19 March 2023
Revised: 28 April 2023
Accepted: 30 May 2023
Published: 3 June 2023
Retracted: 23 April 2024

1. Introduction

The use of unmanned aerial vehicles (UAVs) has become widespread and poses a significant threat to densely populated areas, as well as restricted areas such as airdromes [1,2]. Thermal infrared (IR) imaging allows remote monitoring of drones in all weather circumstances. Thus, the anti-unmanned-drone technique based on a thermal infrared imaging system has received increasing attention from investigators [3,4], while the infrared acquisition of small targets is also an essential technology in military, civil, and other fields [5–7]. This technology plays a crucial part in UAV target detection [8], control, and defense [9]. Quick and exact identification and tracing of targets in each frame is crucial in infrared detection [10]. However, it is challenging to correctly detect the genuine target without false alarms mainly because of the following reasons: (a) In images obtained by the infrared imaging machinery, the small target takes up only a handful of pixels in the entire image.

This paper has been retracted. A retraction notice was published on 23 April 2024 in *Remote Sensing* **2024**, *16*, 1479. https://doi.org/10.3390/rs16091479

The distance between the infrared imaging system and the actual target is usually large, making the small target less noticeable in the overall image with no distinct features or texture [11]. (b) Detecting small IR targets in infrared imaging is challenging due to irregular motion, occlusion, and blurring. The target may only occupy a couple of pixels, making it difficult to tell apart from the background [12]. (c) Complex background edges and high brightness noise with single pixels in the image can often resemble small targets, leading to false positive detection results [13]. Therefore, achieving accurate real-time detection of small IR targets continues to be a challenging task.

There are several existing methods for small IR target detection, including those based on the spatial domain [14], frequency domain [15], morphology [16], and background estimation [17]. While traditional algorithms have been widely used, there is now an increasing interest in deep-learning-based techniques, both supervised [18] and unsupervised [19]. The spatial local contrast formula employs the principle of human vision to prioritize the correlation between the target and its surroundings. It computes the local contrast between the target area and its neighboring background to detect the target. Examples of this method include the combination of filtering and morphology [20], the sub-block and contrast approach [21], the difference stemming from the Gaussian bandpass filter [22], the multi-scale local contrast method [23], the local contrast measure map [24], the minimum mean square means for backdrop estimation [25], and the matched filtering and three-layer windows [26]. Three classifications can be applied to these methods: ratio, differential, and ratio–differential methods. From the discussion in the references, it is evident that ratio-based approaches can enhance the real target but cannot remove a prominent background. Difference-based methods can eliminate a prominent background, but they do not provide an effective way to strengthen the target. Ratio–differential methods can amplify the target while eliminating a high-brightness background. Complex backgrounds can lead to false alarms when using local basic contrast algorithms for detection. However, local contrast algorithms with weighting functions can improve detection performance by suppressing clutter. Some researchers have used local statistics, such as variance or similarity measures, as weighting functions. For example, in [27], a weighting function is created to address cloud edges; in [28], the variance of the central cell is utilized; in [29], the similarity of the target's pixels is combined with the differences between real objectives and their surrounding neighborhood; in [30], the higher signal-to-clutter ratio is applied. On the flip side, some researchers have preferred to design and compute the weighting function themselves. For example, Qi et al. [31] employed the differences between the real object and its neighborhood to create the weight in small image areas. Chen et al. [32] recommended a methodology based on top hat filtering and contrast. Bai et al. [33] improved the entropy formula and proposed a target measurement method of contrast. Nasiri et al. [34] introduced a target area model based on three-layer patches, which utilizes the variance difference between layers. Gao et al. [35] also utilized differences in variance. Liu et al. [36] considered the number of bright pixels in the surroundings. Lv et al. [37] defined a weight function using the regional intensity level between the target and its surrounding neighborhood. Weighted local contrast algorithms typically rely on either a ratio-based or a difference-based approach. While effective, these algorithms have certain limitations as they only consider the difference operation in their weighting function calculation, neglecting the ratio operation, which can result in weak enhancement of the true target. Additionally, some weighting functions may be overly sensitive to random noise, which can lead to the incorrect identification of random noise in a sub-block as a true target, even if it has the highest value. Therefore, a combination of ratio-based and difference-based approaches, known as the ratio–difference combined type, may be more effective.

Over the past decade, deep learning has witnessed remarkable advancements across various domains such as biology, images, speech, language, and more. Numerous researchers have endeavored to synergize local contrast algorithms with neural networks to attain enhanced detection outcomes. Dai and Wu [38] leveraged the scarcity of the target and the self-correlation of the background to effectively segregate the target from the surroundings, employing a tensor structure to design a weight function. In [39], the authors integrated partial tensors and kernel norms to jointly weigh the l1 norm. Gupta et al. [40] introduced a computationally efficient CNN framework and integrated lightweight networks for small target detection. Dai et al. [41] incorporated contrast features into the network feature layer and fused shallow and deep features to achieve target detection. In [42], the authors proposed a framework that combines handcrafted features and convolutional features to extract target features. Similarly, Du et al. [43] devised small anchors for capturing targets based on the shallow layer of the ResNet50 framework. Despite these advancements, FPGA implementation of deep-learning-based methods encounters challenges due to model complexity. Even if deep learning approaches are deployed on FPGA, ensuring real-time performance becomes arduous, thereby impeding the system's ability to provide prompt feedback. Furthermore, training neural network models necessitates substantial data volumes, and a multitude of parameters, and entails high time complexity, resulting in limited generalization capabilities. Considering these factors, the practical utilization of deep learning algorithms in real-world product applications remains limited. Consequently, this study primarily focuses on parsing algorithms that facilitate subsequent hardware processing.

Based on the human visual contrast mechanism, we propose a weighted contrast local contrast method. This algorithm effectively eliminates various clutter and point noise, making it suitable for detecting small targets amidst different background noises. It demonstrates robustness even when the size of the target changes. Furthermore, this algorithm does not require preprocessing and exhibits good robustness. It does not rely on extensive data for a specific network model and possesses the ability for parallel execution. This allows for real-time feedback in target detection systems and facilitates easy productization to address industry needs.

In summary, the main objectives of this study are as follows: (1) to design a contrast method that combines ratio and difference operations to inhibit background noise and enhance target detection; (2) to introduce a novel weighting function, to further restrain random noise; and (3) to design multi-scale operations to accommodate targets with varying sizes.

2. Proposed Method

We begin by analyzing the traits of the target and the different background types depicted in Figure 1. Subsequently, leveraging these characteristics, we present a weighted ratio–difference local contrast method, termed WRDLCM.

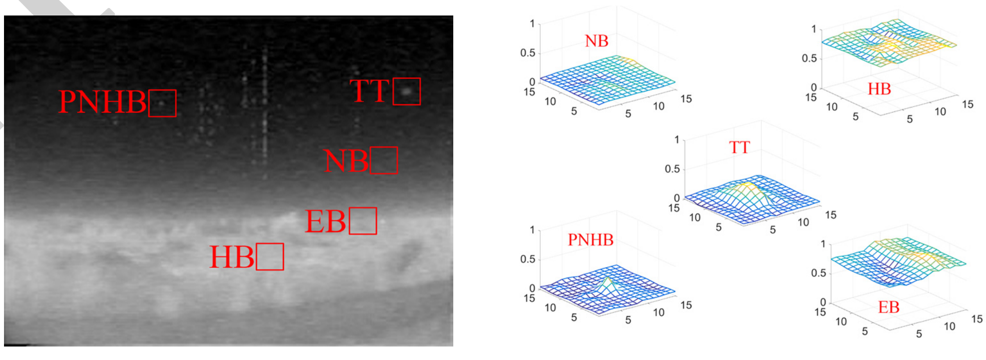

(**a**) (**b**)

Figure 1. (**a**) A really small infrared target with other backgrounds; (**b**) a three-dimensional display of the target and four different types of backgrounds.

2.1. The Characteristics of the Target and Other Different Types of Backgrounds

An IR image containing a small dim target [44] is depicted in Figure 1, encompassing various components: True small target (TT), normal large area background (NB), background with relatively high brightness across the entire image (HB), background with an edge shape (EB), and pixel-sized noises with high brightness (PNHB). The 3D distributions provide a comprehensive visualization of the detailed pixel information for each component. Based on the characteristics observed in both the two-dimensional and three-dimensional images depicted in Figure 1:

(1) A genuine infrared target typically exhibits a concentrated region where pixel values gradually diminish from the center outwards, with a relatively finite number of pixels distributed across the entire image. Leveraging the principles of thermal infrared images, moving targets tend to have higher pixel values compared to the stationary background.
(2) In an infrared image, a normal background typically appears in large quantities, characterized by relatively low pixel values. Conversely, the target pixels exhibit a significantly larger value, rendering it more prominent when contrasted with the normal background.
(3) A high-brightness background often manifests as a largely connected area with substantial pixel values. While these pixel values may exceed those of the real target, the differences in pixel values between highlighted backgrounds are relatively small. Consequently, it becomes easier to distinguish the genuine target from the highlighted backdrop.
(4) When dealing with backgrounds that contain edges, a significant difference is usually noticeable in a particular direction. However, real targets differ from their neighboring elements in all surrounding directions.
(5) The pixel value of PNHB may closely resemble that of a real target. However, PNHB occupies a very limited number of pixels, often just a single pixel, whereas the pixels corresponding to the real target form a circular area with a similar appearance [45].

Based on the above observation results, contrast features can be designed to accurately capture real targets [46,47].

On the basis of analyzing the above objectives and the characteristics of different types of backgrounds, we propose a weighted ratio–difference local contrast method(WRDLCM) consisting of two main components: a fundamental local comparison algorithm and a weight function. The first component entails a ratio-based and difference-based local contrast algorithm that facilitates target enhancement while suppressing the background. The second component involves a weight function, which incorporates the concept of ratio–difference combination. Additionally, to accommodate targets of different sizes, a multi-scale algorithm is devised. Notably, prior to calculating the weight function, we introduce the IRIL approach that suppresses random noise by utilizing the average value of the largest pixels instead of solely relying on the maximum value. This method has proven advantageous in detecting targets moving within complex environments. The proposed algorithm prioritizes a restricted number of pixels within the local small area during the calculation of each pixel, leading to a reduced computational load. Furthermore, the algorithm supports parallel processing techniques, thereby facilitating efficient real-time performance.

2.2. Design of the Detection Algorithm

Based on the preceding analysis, it is established that a truly small target within an infrared (IR) image exhibits notable significance within a limited vicinity of its surrounding neighborhood. Additionally, the pixel value of the target gradually diminishes from the center toward the periphery, while the normal background tends to be dark and featureless. Consequently, it is feasible to concentrate on the localized range encompassing the target and its surroundings, represented by a window (as depicted in Figure 2). We define this confined pixel range as an image block, comprising nine sub-blocks: a central sub-block denoted as T and eight neighboring sub-blocks labeled as B1 to B8. By traversing the entire image using these image blocks, the central sub-block can effectively discern the presence of a genuine target, while the surrounding sub-blocks aid in determining background information. In situations where target measurements are inconclusive, the size of the sub-block, denoted as N, should correspond to the dimensions of the largest small target [22]. According to the international optical organization SPIE, small targets typically exhibit dimensions smaller than 9×9 pixels [48].

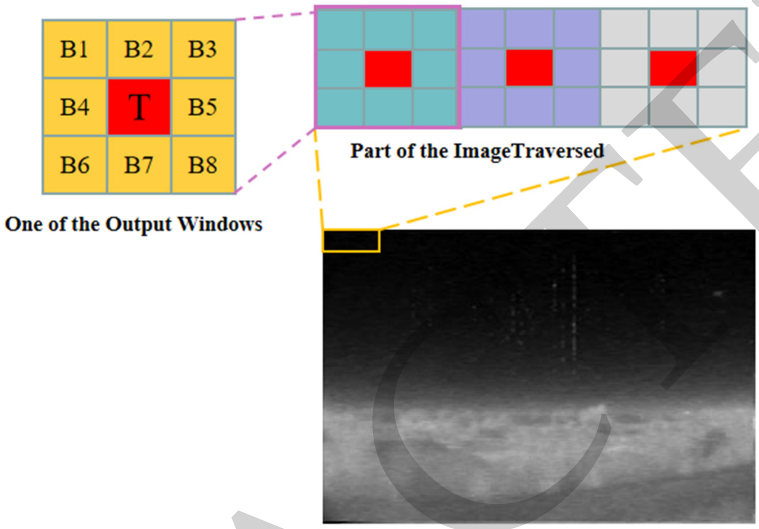

Figure 2. Local small image window used for WRDLCM calculation.

The detailed process of the WRDLCM algorithm is depicted in Figure 3. Initially, for the unknown target, the number of possible scales can be set first, and the contrast can be calculated at each scale, for example, at the pth scale, the local contrast methods of ratio (RLCMp) and difference (DLCMp), as well as the weight function based on the local contrast method (WLCMp), are computed for the window. The RLCMp and DLCMp are then combined to form RDLCMp, which is multiplied by the weighting function to obtain WRDLCMp. Finally, the maximum value across multiple scales is selected as the WRDLCM output. We will describe the multi-scale detection method in Section 2.2.5. By applying a threshold, precise target identification can be achieved.

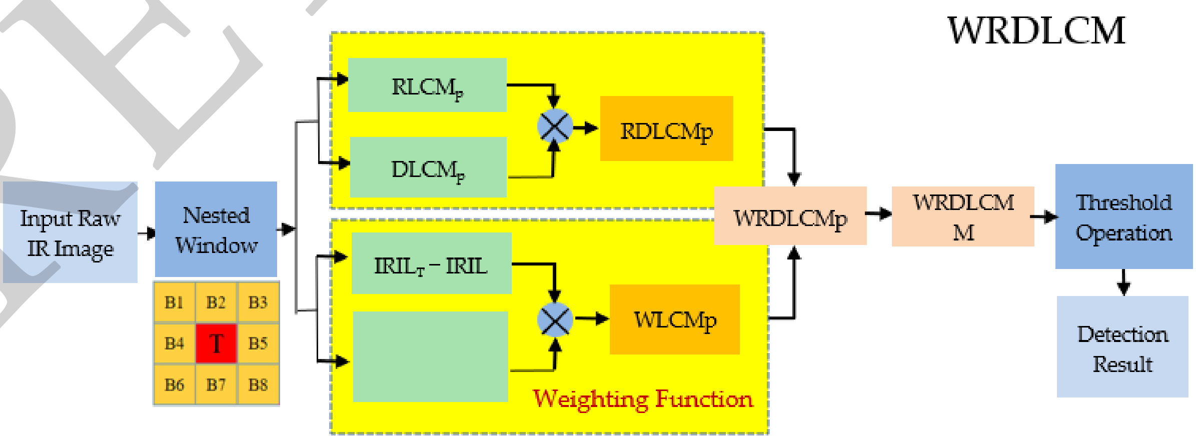

Figure 3. The detailed process of the WRDLCM algorithm.

Traversing the image block through the entire image will ultimately result in a new matrix in which the target will occupy the highlighted pixel portion, and the pixel value of the remaining background portion is 0.

2.2.1. The Calculation of the Radio-Based Local Contrast Method (RLCM)

In many papers, it is common for authors to calculate contrast using the maximum pixel value. However, these approaches may not effectively suppress normal backgrounds or minor noise surrounding the target, leading to inaccurate small target detection. In this article, we propose a different method where contrast is calculated using average pixel values. This approach allows for the elimination of background and clutter, resulting in more accurate small target detection.

In the *i*th direction, the pixel contrast of $\mathrm{RLCM_i}$ between the background sub-block Bi and the center sub-block T is identified as follows:

$$\mathrm{RLCM}_i = \frac{M_T}{M_{Bi}},\ i = 1, 2, \ldots, 8 \tag{1}$$

where

$$M_T = \frac{1}{K_1}\sum_{j=1}^{K_1} Gray_T^j \tag{2}$$

$$M_{Bi} = max\left\{\frac{1}{K_2}\sum_{j=1}^{K_2} Gray_{Bi}^j,\ \xi\right\},\ i = 1, 2, \ldots, 8 \tag{3}$$

here, ξ is a small value greater than 0. In the event that the denominator in the above formula is 0, ξ is set to 1.

K_1 and K_2 represent the maximum number of grayscale values in the sub-block, $Gray_T^j$ and $Gray_{Bi}^j$ denote the *j*th maximal gray value of T and Bi, respectively. The inclusion of mean operations in M_T and M_{Bi} helps mitigate the interference of PNHB. Moreover, considering that the real target typically exhibits attenuation from the center, it is recommended to set K_1 to a value smaller than the pixel count of the target. This choice ensures a larger RLCM value, thereby enhancing the target. Additionally, for better results, it is advisable for K_2 to be slightly larger than K_1.

In the context of the image block illustrated in Figure 2, there are eight directions surrounding the target. To counteract the impact of edge background, the RLCM is described as follows:

$$\mathrm{RLCM} = \min\{\mathrm{RLCM}_i\},\ i = 1, 2, \ldots, 8 \tag{4}$$

2.2.2. The Calculation of the Difference-Based Local Contrast Method (DLCM)

Based on the analysis presented in Section 2.1, it is observed that a high-brightness background typically manifests as a connected region with significantly larger pixel values, exhibiting similarity within the highlighted background area. Exploiting this characteristic, we can devise a differential form of contrast to counter the effects of the highlighted background. The contrast difference in the *i*th direction is defined as follows:

$$\mathrm{DLCM}_i = \max\{|M_T - M_{Bi}|,\ \xi\},\ i = 1, 2, \ldots, 8 \tag{5}$$

where M_T and M_{Bi} are the same as in Formulas (2) and (3), respectively, and ξ is defined as in Formula (3). The absolute value in Formula (5) is used to avoid negative values.

The final DLCM is obtained by selecting the largest DLCM value among the eight neighborhood directions, as expressed by the following equation:

$$\mathrm{DLCM} = \max\{\mathrm{DLCM}_i\},\ i = 1, 2, \ldots, 8 \tag{6}$$

2.2.3. The Calculation of the RDLCM

As discussed earlier, RLCM is effective in handling complex background edges, PNHB, and normal background, while DLCM is capable of eliminating a high-light background and PNHB. To enhance the real target more effectively, we propose a ratio–difference combined local contrast method (RDLCM) that combines the strengths of RLCM and DLCM. By calculating the Hadamard product of RLCM and DLCM, the calculation formula for RDLCM is as follows:

$$\mathrm{RDLCM} = \mathrm{RLCM} \circ \mathrm{DLCM} \tag{7}$$

2.2.4. Definition of the WLCM

(1) The Improved RIL

In scenarios where the image contains multiple backgrounds and significant clutter, relying solely on RDLCM for detection may lead to false alarms. To address this challenge, this paper introduces a novel weighting function that comprises two components. The first component involves the introduction of the IRIL, which aims to mitigate the impact of clutter and enhance target detection accuracy. The second component focuses on the computation of the weighting function based on the ratio–difference combination. Together, these components contribute to improving the detection algorithm's overall effectiveness.

The RIL introduced by Lv et al. [41] is a valuable metric for evaluating the intricacy of a block. However, the initial RIL definition, sensitive to isolated random noise, is merely determined as the difference between the block's highest value and its mean value. To address this limitation, we propose the IRIL, which incorporates the mean value to mitigate the impact of isolated random noise. This improved definition applies to both the IRIL_i of neighborhood sub-blocks Bi and the IRIL_T of the center sub-block T.

$$\mathrm{IRIL}_T = M_T - T_{mean} \tag{8}$$

$$\mathrm{IRIL}_i = M_T - B_{imean},\ i = 1,\ 2,\ \ldots,\ 8 \tag{9}$$

$$\mathrm{IRIL} = \max\{\max\{|M_{Bi} - B_{imean}|,\ \xi\}\},\ i = 1,\ 2,\ \ldots,\ 8 \tag{10}$$

where M_T and M_{Bi} are the same as Formulas (2) and (3), respectively. The subscript "mean" indicates the average value. The absolute value in Formula (10) is used to ensure non-negativity. ξ is the same as in Formula (3). The results of M_T and M_{Bi} from Formula (2) and Formula (3) can be directly utilized without precomputation, which greatly enhances efficiency. The final IRIL value is obtained through the maximum pooling procedure.

(2) The WLCM

In this paper, similar to the calculation method of the RDLCM, The WLCM is computed using both ratio and difference operations. IRIL_T and IRIL are incorporated as weighting factors to calculate the ratio and difference, respectively. The weight value $w(x,\ y)$ of a specific pixel $(x,\ y)$ is obtained as follows:

$$w(x,\ y) = \frac{\mathrm{IRIL}_T}{\mathrm{IRIL}} \circ (\mathrm{IRIL}_T - \mathrm{IRIL}) \tag{11}$$

$$\mathrm{WLCM} = \max\{0,\ w(x,\ y)\} \tag{12}$$

When defining WLCM, we take into consideration non-negative constraints to ensure that the weight function remains positive. The weighting function in this study is designed based on the similarities and differences between the target and background. Compared to existing weight function approaches, it incorporates a wider range of factors, providing a more comprehensive representation. Algorithm 1 shows the calculation steps of WRDLCM at the pth scale.

Algorithm 1 WRDLCM computation at the *p*th scale

Input: Raw IR image and the parameters N, K_1, and K_2.
Output: The result of the **WRDLCMp** calculation is a matrix called **WRDLCMp**.
1: Create a patch consisting of 9 cells, as depicted in Figure 2.
2: Translate the patch horizontally in a left-to-right motion and vertically from top-to-bottom over the raw IR image.
3: At every pixel, compute its corresponding **RLCMp** and **DLCMp** values using formulas (1)–(6).
4: Once the calculation is completed for the entire image, create two new matrices **RLCMp** and **DLCMp** to store the results.
5: Standardize the constituents in **RFLCMp** to the range (0, 1).
6: Standardize the elements in **DFLCMp** to the range (0, 1).
7: Compute the **RDLCMp** of the raw IR image by taking the Hadamard consequence of **RLCMp** and **DLCMp**:
8: Compute the **WLCMp** of the raw IR image using formulas (8)–(12).
9: Standardize the parts in **WLCMp** to the range (0, 1).
10: Determine the **WRDLCMp** of the raw IR image by performing the Hadamard outcome of **RDLCMp** and **WLCMp**.

2.2.5. Multi-scale WRDLCM Calculation

The previous basic contrast algorithm and weight function are multiplied using the Hadamard product to form WRDLCM, as shown in Equation (13). This operation effectively enhances small targets throughout the entire image. The contrast calculation for each window is performed in parallel, improving the program's runtime speed and satisfying the real-time demands of the probing system.

$$\mathrm{WRDLCM} = \mathrm{RDLCM} \circ \mathrm{WLCM} \tag{13}$$

Regarding the key parameter K in Formulas (2) and (3), achieving multi-scale target detection requires self-adaptive adjustment based on the target's size. By applying Formulas (1) to (13), the WRDLCM can be determined, and the WRDLCM values at different scales can be maximized. The formula is as follows:

$$\mathrm{WRDLCM} = \max\left\{\max\left\{\mathrm{WRDLCM}_p\,,\ p = 1,\ 2,\ \ldots,\ L\right\},\ 0\right\} \tag{14}$$

The range of p is 1 to L, representing the first scale, the second scale, and so on. L represents the number of scales. It is important to note that real targets are typically brighter than their surrounding objects. To further suppress clutter, non-negative constraints are applied.

The process of multi-scale WRDLCM calculation can be described as follows:

(1) For the pth scale, suitable values of K_1 and K_2 are selected. In this paper, three scales are designed. For scale 1 (target size 3×3), the values of K_1, K_2, and N are configured to 2, 4, and 5, respectively; for scale 2 (target size 5×5), the values of K_1, K_2, and N are configured to 9, 18, and 7, respectively; for scale 3 (target size 7×7), the values of K_1, K_2, and N are configured to 16, 32, and 9, respectively.
(2) For a given IR image, the output of the maximum WRDLCM at each pixel across different scales is determined using Formula (14). It can be easily demonstrated that performing multi-scale WRDLCM calculation yields the most appropriate detection results. Furthermore, this algorithm incorporates parallel operations during the contrast calculation, significantly optimizing the real-time performance of the detection system.

Algorithm 2 gives the main steps of the multi-scale WRDLCM calculation.

Algorithm 2 multi-scale WRDLCM determination

Input: Raw IR image and the parameters N, K_1, K_2, . . . , K_L. for L scales.
Output: The resulting matrix of the **WRDLCM** calculation is called WRDLCM.
1: **for** p = 1,2, . . . ,L **do**
Compute the WRDLCM_p using K_p based on **Algorithm 1**.
2: **end for**
3: For each pixel, output the highest **WRDLCM** value across all L scales as the final multi-scale **WRDLCM** value, denoted as:

$$\mathrm{WRDLCM} = \max\{\max\{\mathrm{WRDLCM}_p\ ,\ p = 1,\ 2,\ \ldots,\ L\},\ 0\} \quad (14)$$

where (i, j) is the location of each pixel.

3. Performance Analysis and Threshold Manipulation

3.1. Analysis of Detection Performance

Figure 4 shows image blocks in various regions in the original IR image. The left side of each graphical block represents its 3D distribution. Specifically, Figure 4a illustrates a region containing a genuine small target, while the remaining sub-images showcase different types of backgrounds.

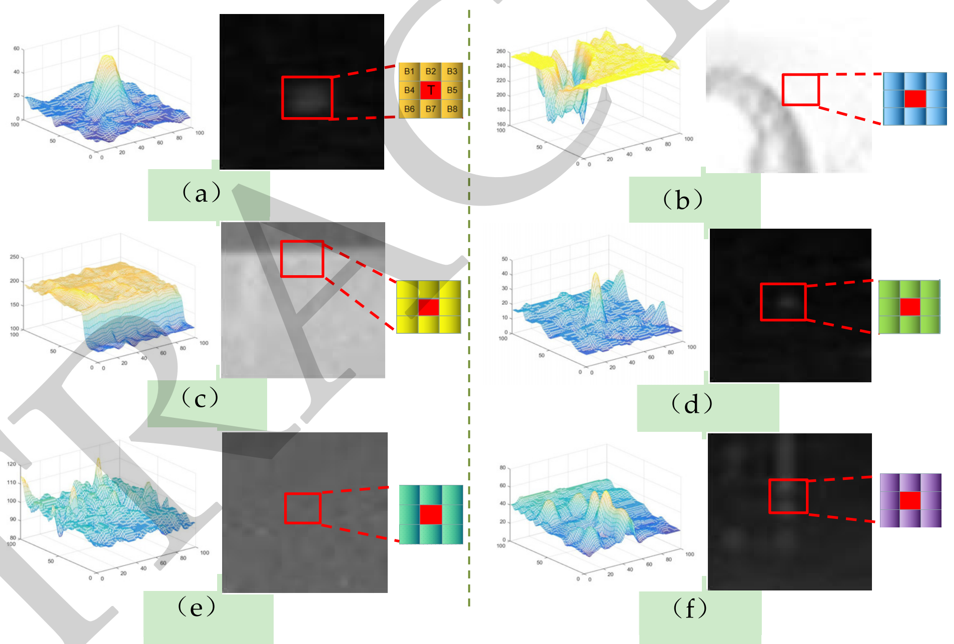

Figure 4. Image blocks in different regions in the original infrared image: (**a**–**f**) represent the real small target, highlighted background, edge background, point noise, normal background, and pulse noise in sequence, respectively.

A thorough observation of the 3D distribution map in Figure 4 reveals distinct characteristics for both the target and each background type. By employing the ratio and difference calculations in the algorithm, it can be deduced that only the WRDLCM of the real target yields the highest value. Consequently, this analysis demonstrates the capability to accurately detect small targets.

3.2. Threshold Operation

After the computation of WRDLCM, the target becomes highly prominent in the image, while the majority of the background is filtered out. Subsequently, the employment of threshold operations enables the extraction of the genuine target. The formula for determining the threshold value is as follows:

$$\mathrm{Th} = \lambda \cdot \max(\mathrm{WRDLCM}) + (1 - \lambda) \cdot \mathrm{mean}(\mathrm{WRDLCM}) \quad (15)$$

where λ is a given factor between 0 and 1.

During our analysis of experimental results, we determined that an appropriate range for the threshold parameter λ lies between 0.6 and 0.9. Utilizing the WRDLCM results, we solely extract the portion where the pixel value exceeds the threshold. To enhance the displayed outcome, we further apply an expansion operation to the extracted region. The output result of the algorithm comprises the small target along with its expanded region.

4. Experimental Analysis and Results

To validate the algorithm proposed in this article, we conducted experiments using various infrared small target datasets. All experiments were conducted on a 2.70 GHz Intel Core i5-6400 PC with 8 GB of RAM under MATLAB environment.

4.1. Data and Performance Evaluation Indicators

In this paper, the number of scales we utilized is three, and the size distribution of N is set to 5×5, 7×7, and 9×9, respectively. We conducted tests on infrared images consisting of 1400 frames from multiple sequences. These sequences encompassed varying sizes of small targets and distinct backgrounds. Table 1 offers a general outline of the first frame image of each sequence. Some of these sequences were captured by HgCdTe infrared detectors, and depict floor plans near Wuhan Tianhe International Airport, while the remaining images were provided by our team.

Table 1. Description of 6 real infrared sequences.

Sequence	Frames	Size	Target Number	Target Size	Target Type
Seq. 1	200	320 × 256	1	2 × 3~3 × 4	Plane
Seq. 2	300	256 × 256	1	3 × 3~3 × 4	Drone
Seq. 3	300	256 × 256	1	3 × 5	Truck
Seq. 4	200	320 × 256	1	3 × 5	Plane
Seq. 5	200	320 × 256	1	4 × 5	Plane
Seq. 6	200	320 × 256	1	3 × 3	Plane

We use the common signal clutter ratio gain (SCRG) and background suppression factor (BSF) to evaluate the capability of the algorithm. Higher values of these performance indicators indicate better performance. SCR stands for signal-to-noise ratio. A small target with a higher SCR is more easily detectable. SCRG measures the level of enhancement of the input and output signals of a target in comparison to the background. It is also an indicator of the difficulty of detecting small targets. SCR and SCRG are established as follows:

$$\mathrm{SCR} = \frac{|\mu_t - \mu_b|}{\sigma_b},\ \mathrm{SCRG} = \frac{\mathrm{SCRG}_{\mathrm{out}}}{\mathrm{SCRG}_{\mathrm{in}}} \tag{16}$$

where μ_{t} signifies the average pixel size of the target, μ_{b} represents the pixel value size of the area around the target, and σ_{b} is the standard deviation of pixel values around the target. $\mathrm{SCRG}_{\mathrm{in}}$ indicates the signal-to-noise ratio of the input image, and $\mathrm{SCRG}_{\mathrm{out}}$ epitomizes the signal-to-noise ratio of the output image.

BSF indicates the efficacy of background attenuation, and the formula is as follows:

$$\mathrm{BSF} = \frac{C_{in}}{C_{out}} \tag{17}$$

where C_{in} signifies the deviation from the mean of the original input image, and C_{out} symbolizes the deviation from the mean of the output image after detection.

4.2. Experimental Outcomes Using the Proposed Method

In Figure 5a, we present samples from six sequences where the real target is not prominent in the entire image, occupying only a few pixels, with significant interference surrounding it. Figure 5b showcases the calculation output of RLCM (displaying a single-scale result with a block size of 5 × 5). Figure 5c displays the results of DLCM, while Figure 5d demonstrates the joint operation of RLCM and DLCM, resulting in RDLCM. Compared to Figure 5b, Figure 5d effectively filters out most of the background, making the infrared target more salient. The effect of the weight function WLCM, designed in this paper, is displayed in Figure 5e. Figure 5f showcases the combined performance of WLCM and WRDLCM. In Figure 5g, the target becomes more prominent, and the background is nearly suppressed due to the influence of the weight function. Finally, accurate detection of the actual target is achieved through threshold operations, as depicted in Figure 5h.

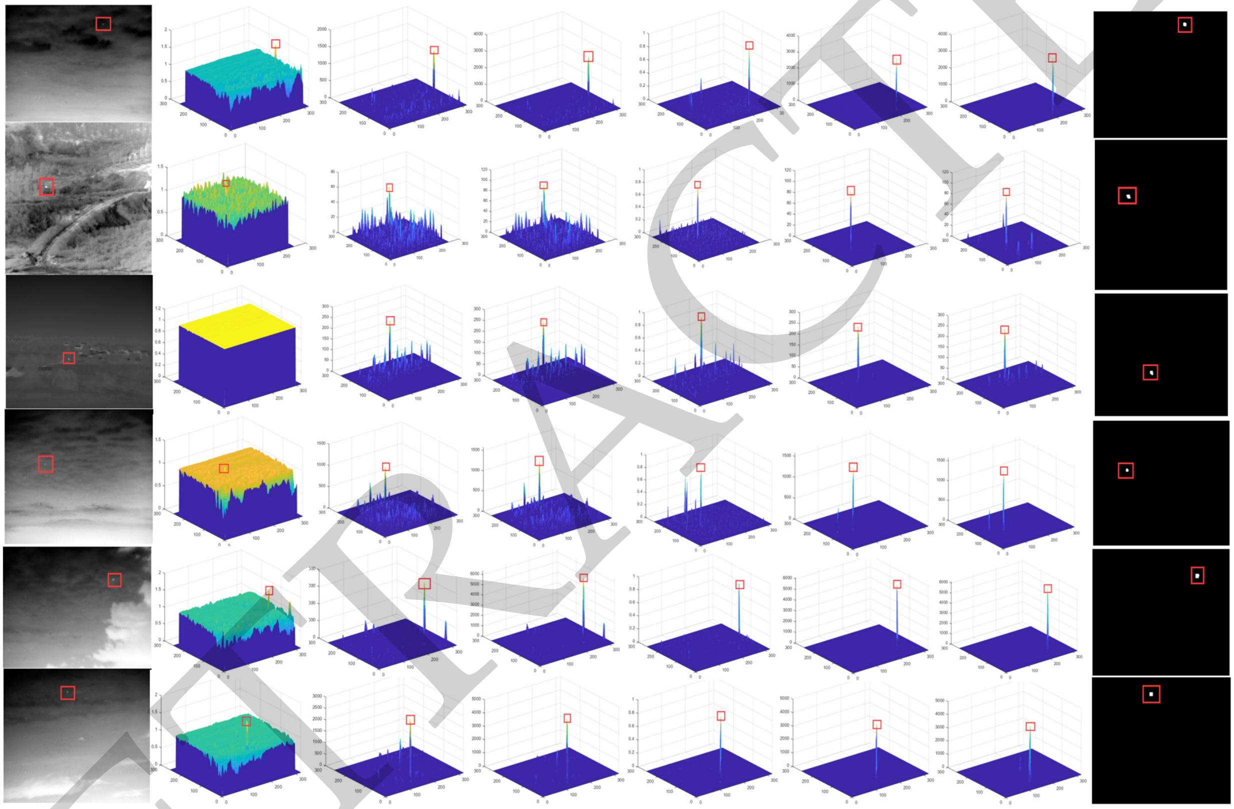

(a) (b) (c) (d) (e) (f) (g) (h)

Figure 5. The result of contrast calculation at each step of the algorithm for the six sequences: (**a**) original infrared image; (**b**–**f**) calculation results of RLCM, DLCM, RDLCM, WLCM, and WRDLCM at the same scale, respectively; (**g**) results of maximizing WRDLCM at multiple scales; and (**h**) threshold screening and detection results after expansion.

To assess the adaptability of the proposed algorithm to the real-time motion of infrared targets, we conducted tests on randomly selected images from the aforementioned six sequences (excluding the images used in Figure 5). The results, presented in Figure 6, demonstrate that even with random image selection within the sequence, the algorithm reliably detects the real target. This further confirms the effectiveness of the algorithm and its ability to adapt to varying scenarios.

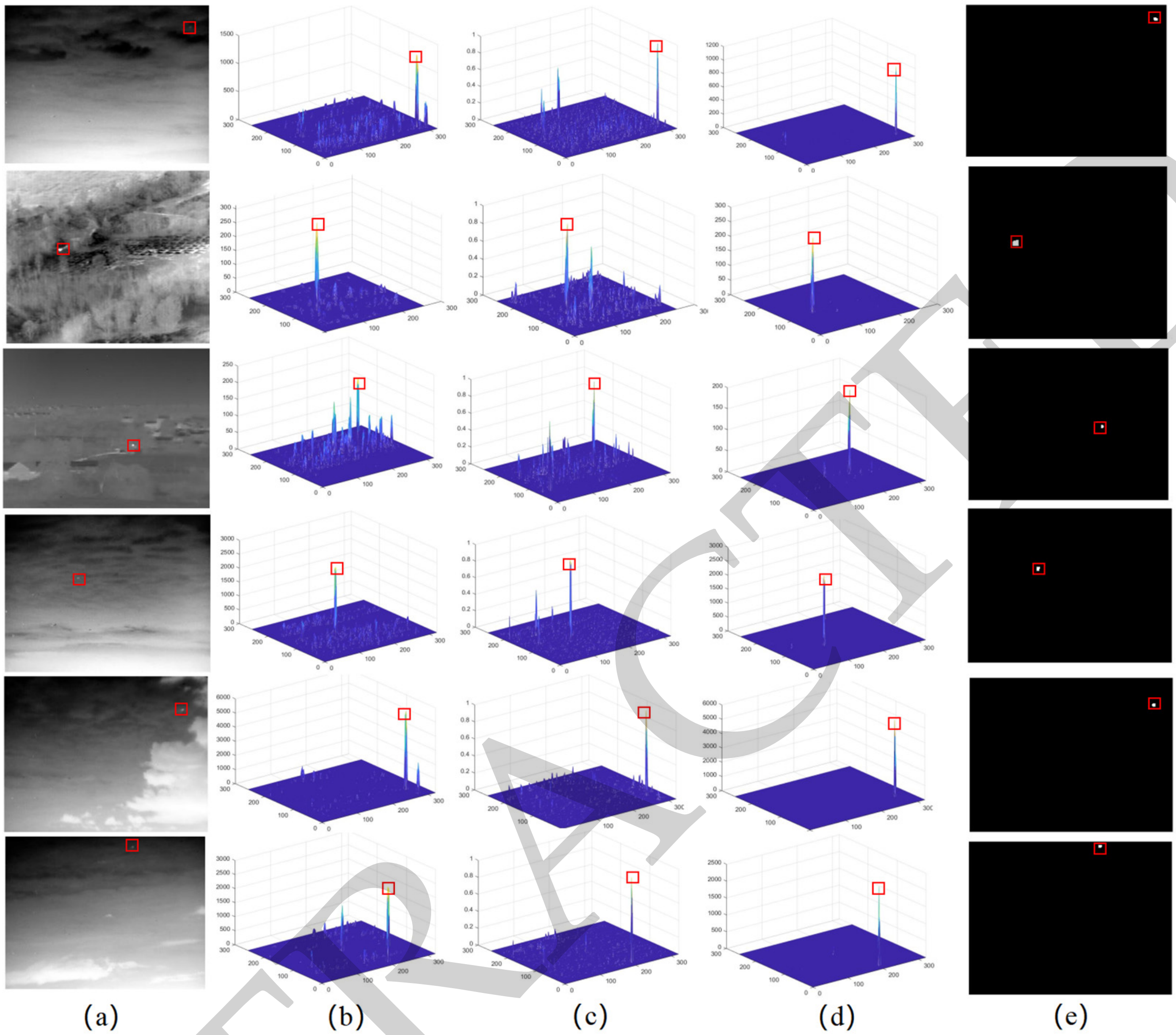

Figure 6. Step test results of sample images randomly selected from six sequences: (**a**) original infrared image; (**b**,**c**) calculation results of RDLCM and WLCM at the same scale, respectively; (**d**) the results of maximizing WRDLCM at multiple scales; and (**e**) threshold screening and detection results after expansion.

4.3. Comparisons with Popular Methods

The algorithms that were compared to our proposed algorithm include VAR-DIFF [6], ILCM [21], NLCM [22], MPCM [24], RLCM [23], MDTDLMS [25], and WLDM [27]. The VAR-DIFF algorithm incorporates a weight function in its contrast calculation, but it only utilizes a difference operation. ILCM and MPCM are sub-block-based methods without weighting. The RLCM and MDTDLMS algorithms employ both difference and ratio operations. The weight functions in WLDM and NLCM are designed based on specific characteristics of small targets. Our proposed algorithm, WRDLCM, introduces a novel approach combining ratio–difference operations and a new weighting function.

Tables 2 and 3 present a thorough comparison of different algorithms using two widely adopted performance metrics: SCRG and BSF. Higher values of these performance indicators indicate better performance. Our algorithm demonstrates significant improvement in enhancing genuine targets, leading to favorable SCRG and BSF values across most scenarios.

Table 2. The SCRG of different algorithms.

Seq	VAR-DIFF	ILCM	NLCM	MPCM	RLCM	WLDM	MDTDLMS	SBE	WSLCM	Proposed
1	81.0621	46.9499	44.121	8.3706	20.1072	96.6349	134.0081	141.6602	158.2621	187.4666
2	28.589	3.9251	7.8695	1.5108	3.3806	8.1257	11.9812	13.9991	23.7546	27.4135
3	7.9416	1.9404	1.6612	2.0665	1.5181	19.0926	3.6358	8.3069	9.7639	12.43
4	24.4902	13.0714	18.8765	2.8125	11.8627	46.2286	48.9359	102.9054	91.9173	150.8203
5	69.4871	7.4718	10.3798	6.2368	13.2762	75.9957	59.4319	56.0565	52.0043	67.2493
6	67.6344	8.8442	11.6066	6.2767	15.3084	124.8624	66.1583	81.0356	79.2109	141.4133

Table 3. The BSF of different algorithms.

Seq	VAR-DIFF	ILCM	NLCM	MPCM	RLCM	WLDM	MDTDLMS	SBE	WSLCM	Proposed
1	5.04×10^{-10}	46.3694	0.022	0.0192	15.1353	22.8578	3.89×10^{5}	6.33×10^{5}	0.0366	5.54×10^{5}
2	3.77×10^{-5}	7.9812	0.0943	0.1349	2.4911	37.9672	1.64×10^{3}	2.03×10^{3}	0.0218	3.91×10^{3}
3	7.45×10^{-9}	9.1742	0.0344	0.1368	2.1982	16.5951	4.24×10^{3}	1.13×10^{4}	0.1694	7.67×10^{3}
4	2.85×10^{-10}	49.5869	0.0361	0.0202	11.12	15.1272	1.35×10^{5}	3.12×10^{5}	0.0638	4.09×10^{5}
5	2.49×10^{-11}	25.8584	0.0052	0.0107	7.7217	12.5982	3.69×10^{5}	5.94×10^{5}	3.61×10^{-4}	4.16×10^{5}
6	8.00×10^{-11}	34.5385	0.0059	0.0261	9.1028	18.5719	4.70×10^{5}	3.89×10^{5}	0.002	4.08×10^{5}

VAR-DIFF performs well from the perspective of SCRG and BSF in the second and third sequences but shows limited performance in the remaining sequences. The differential operation in VAR-DIFF can effectively eliminate backgrounds with large areas of similar pixel values and accurately detect genuine targets. However, it struggles to suppress complex backgrounds in the presence of bright backgrounds or clutter, resulting in a subpar performance in the other four sequences. ILCM, NLCM, MPCM, and RLCM all exhibit low SCRG and BSF values, as these methods do not employ weight functions to enhance targets. They simply rely on differential or ratio–difference combined contrast for target detection. WLDM, on the other hand, incorporates a weight function to enhance targets and demonstrates high SCRG values in the third, fifth, and sixth sequences, as its designed weight function effectively resists cloud edges. MDTDLMS combines the concepts of background estimation and difference ratio, and exhibits excellent SCRG performance in the first sequence due to the simplicity of the background, which allows for accurate estimation. However, its performance in other sequences is not as strong as that of our proposed method. Based on the calculation results, our proposed method demonstrated superior performance in comparison to most methods, consistently achieving outstanding SCRG and BSF values across all six sequences. Although the SBE method may have outperformed our algorithm in certain sequences, its algorithmic complexity surpasses that of our proposed method.

The receiver operating characteristic (ROC) curve is an important measure for evaluating the capability of an algorithm. It gives a graphical depiction of the relationship between the true positive rate and the false positive rate. Figure 7 presents the comparison of ROC curves for different algorithms. In addition to the aforementioned comparison algorithms, several additional methods are included in the ROC curve comparison, such as TLLCM [26], STLCM [49], TCF [50], STLCF [51], SBE [52], and WSLCM [53], which are popular algorithms of different types. From the ROC curve, it is evident that our proposed method outperforms most algorithms and is comparable to newer approaches developed in recent years.

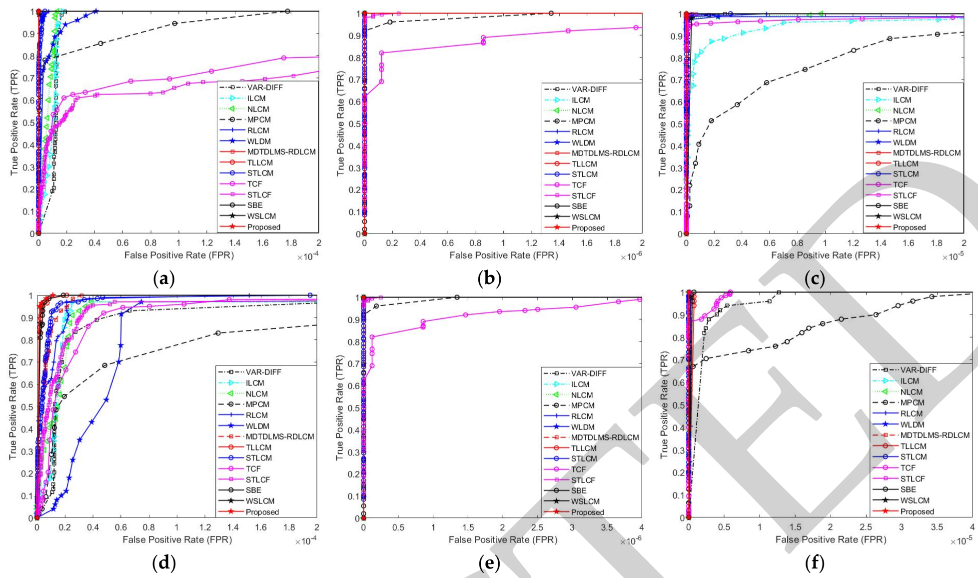

Figure 7. ROC curves of detection effect under different algorithms: (**a**–**f**) Seq.1–Seq.6.

To evaluate the capability of the algorithm, we conducted tests on both a real dataset and a simulated dataset consisting of 200 infrared images containing small targets and complex backgrounds. The simulation parameters were set as follows: an image size of 256 × 320 pixels, a signal-to-noise ratio of 0.2, a background brightness of 100, a target brightness of 120, and a bright region in the upper left corner of the simulated image with a brightness value of 150. The initial target coordinates on the first frame were set to 80 on the vertical axis and 20 on the horizontal axis. The horizontal positions were incremented by 1 for each subsequent frame. The target's shape was generated using a two-dimensional Gaussian model. The target and background were combined to create the simulated image, and random noise with a noise intensity of 20 was added.

Subsequently, the performance of the proposed algorithm was tested on this simulated dataset, and several comparative algorithms were also applied to assess the dataset and generate ROC curves. Figure 8 illustrates the challenges posed by the bright background and complex noise in the vicinity of the target, making target detection difficult. We tested the images from the 200 datasets and selected two random images to showcase the detection results. As depicted in Figure 8, small targets can be accurately detected even in the presence of complex bright backgrounds and noise.

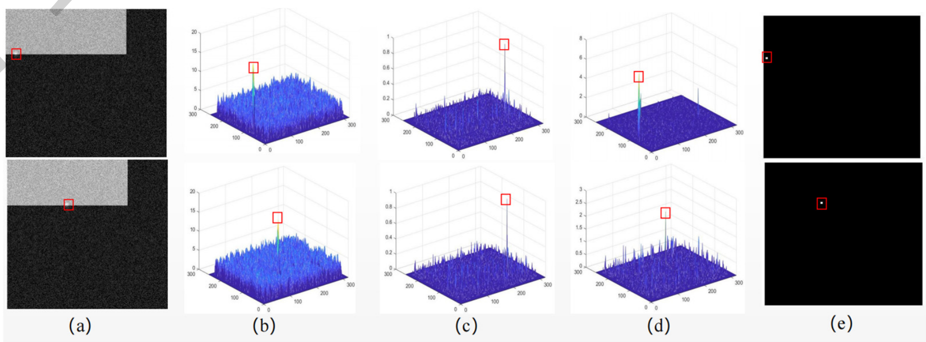

Figure 8. Contrast calculation results at the main steps of the algorithm for the simulated images: (**a**) simulated images; (**b**,**c**) calculation results of RDLCM and WLCM at the same scale, respectively; (**d**) results of maximizing WRDLCM at multiple scales; and (**e**) threshold screening and detection results after expansion.

Figure 9 presents the comparison results of the ROC curves for several popular algorithms on the simulated dataset. Our algorithm ranked second in terms of performance. The optimal MDTDLMS-RDLCM [25] algorithm, which combines background estimation and local contrast design, achieved the best performance. This demonstrates the practicality of our algorithm in real-world scenarios. In future work, we can explore the integration of background estimation to design local contrast more suited for target detection. Overall, our algorithm is applicable for detecting small targets in both real and simulated scenarios.

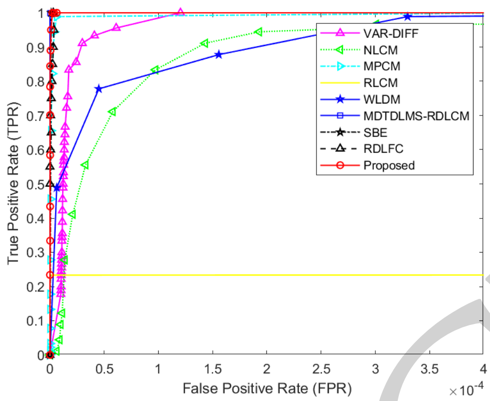

Figure 9. ROC curve of detection effect under different algorithms.

4.4. Experiments against Random Noise

Random noise is a significant factor that can degrade detection performance. To assess the robustness of our algorithm, we introduced different levels of noise to the original images from the sequence used in the previous experiments. Figure 10 illustrates the results where white noise with a variance of 0 and mean values ranging from 1 to 5 was added to the images. Subsequently, a performance test for target detection was conducted. From the ROC curve results presented in Figure 10, it is evident that our proposed algorithm performs well across all noise conditions. Regardless of the varying levels of noise, our algorithm consistently demonstrates reliable detection capabilities.

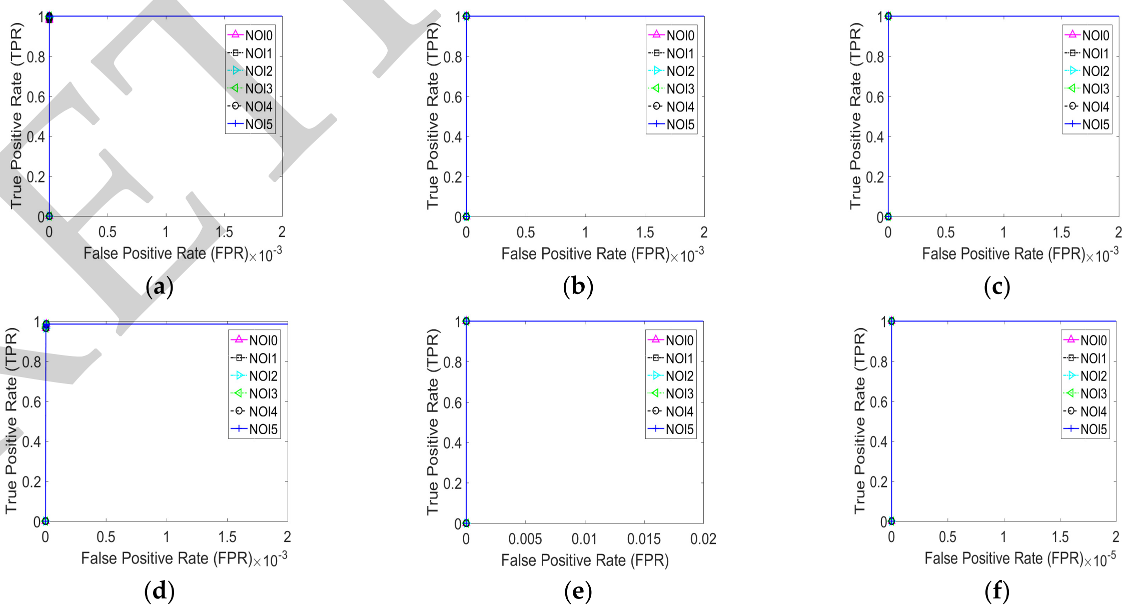

Figure 10. ROC curves of detection effect under different noise levels: (**a**–**f**) Seq.1–Seq.6.

Table 4 provides a comparison of the processing times between several deep learning methods and our proposed approach. The results demonstrate that our method is capable of processing a higher number of frames per unit of time, effectively meeting the real-time requirements. By contrast, deep learning methods such as RIPT [38], PSTNN [39], and MF-LWCNN [40] require more time for processing.

Table 4. Processing frame time for different algorithms.

Method	Frame Size	Time	Platform
RIPT [38]	255 × 320/200 × 256	2.26	CPU
PSTNN [39]	128 × 128/256 × 200/320 × 240	0.49	CPU
MF-LWCNN [40]	300 × 300	0.20	CPU
Our method	320 × 256/256 × 256	0.11	CPU

4.5. Testing of Multiple Targets

To further analyze the effectiveness of our proposed method, we conducted experiments using a sequence containing multiple frames to detect two infrared small targets. Specifically, we utilized Seq.7, which consists of 200 frames, with the background primarily comprising a sea scene. The small targets in the images represent ships, and the image size is 280 × 228. The target sizes range from 5 × 5 to 7 × 7.

Figure 11 illustrates the detection results for two targets. The experimental outcomes validate the capability of our proposed method in highlighting the targets amidst intricate backgrounds. The WRDLCM calculation enhances the visibility of the targets, and the subsequent weighted processing significantly filters out the majority of the background, further emphasizing the targets. By applying a threshold value, the actual targets can be accurately identified.

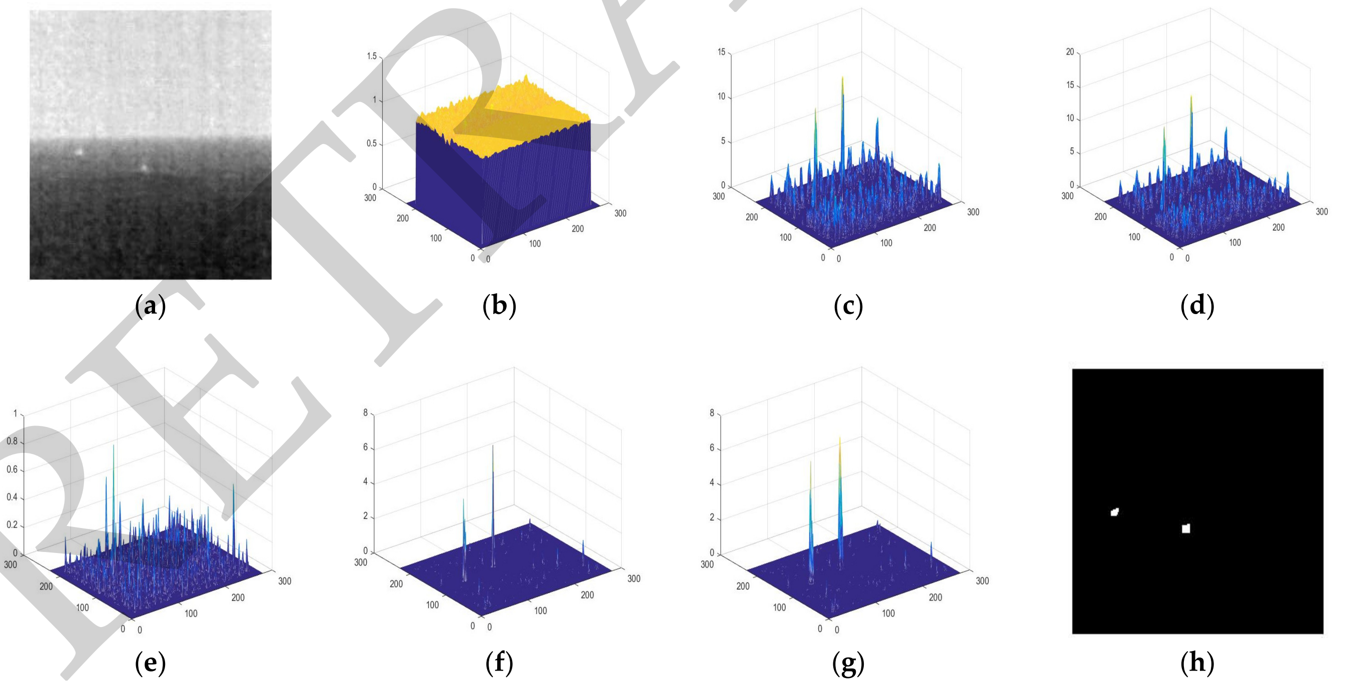

Figure 11. The detection effect of each algorithm step for Seq. 7: (**a**) the raw IR images; (**b**) RLCM; (**c**) DLCM; (**d**) RDLCM; (**e**) WLCM; (**f**) WRDLCM; (**g**) the final multi-scale WRDLCM result; and (**h**) the detection result after the threshold operation.

Figure 12 showcases the detection results of Seq.7 with the addition of random noise. As depicted in Figure 12c, the original image becomes blurred, and the identification of small targets becomes more challenging. Despite the difficulty introduced by the noise, the ROC curve demonstrates the stable performance of our proposed algorithm. However, when the noise variance reaches 8, which is relatively strong, the ROC curve exhibits a slight decrease. This indicates that our algorithm maintains good performance even in the presence of severe noise interference.

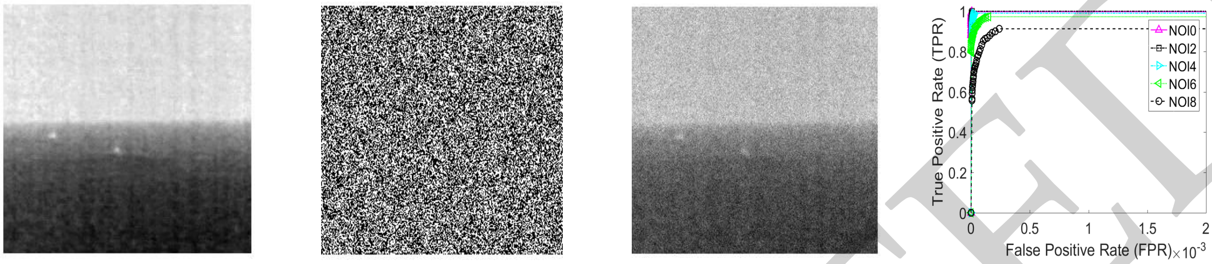

Figure 12. Performance at different noise levels: (**a**) the raw IR image; (**b**) Gaussian noise; (**c**) infrared image with Gaussian white noise (Variance: 8); and (**d**) ROC curves under different levels of random noise.

Furthermore, we conducted performance tests on single-frame images sourced from the single-frame dataset [53] and the public SIRST dataset [54]. These single-frame images allow us to assess the algorithm's capability when spatiotemporal information from consecutive frames cannot be utilized. As depicted in Figure 13, our method achieves accurate target detection even with single-frame images.

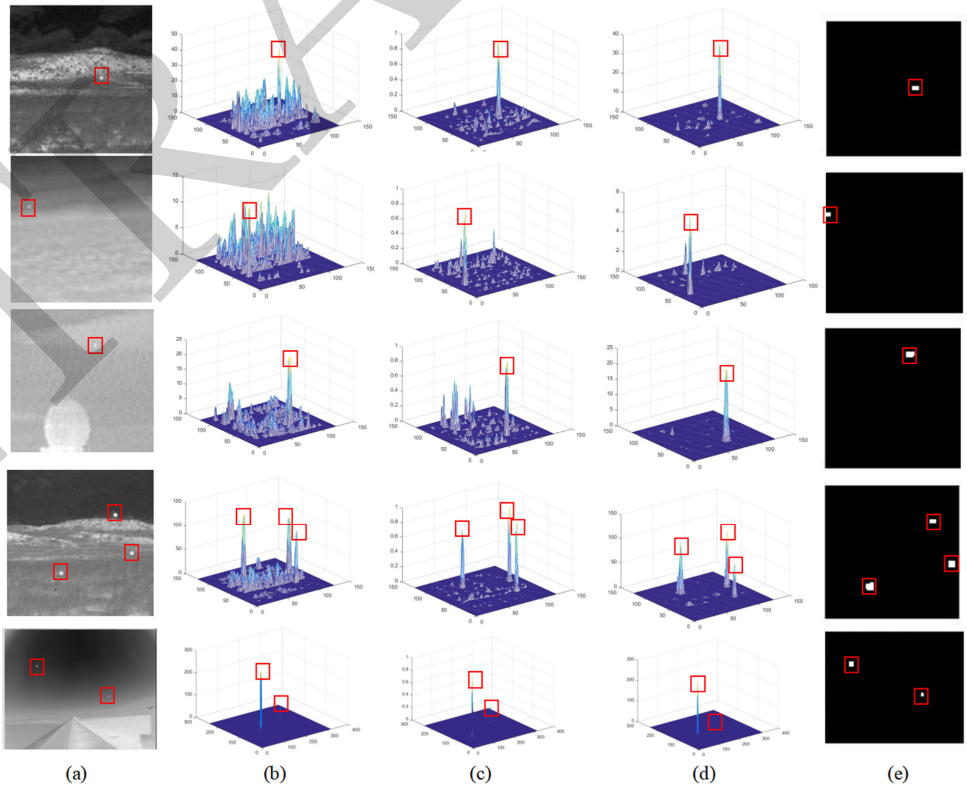

Figure 13. The 3D graphs of the detection results of each step of our device for the single-frame image: (**a**) original; (**b**) RDLCM; (**c**) WLCM; (**d**) WRDLCM; and (**e**) output.

4.6. Detection of Small Inland UAV Targets Using Infrared Images

The accurate detection of small UAV targets holds great significance in both the military and civilian domains. This section focuses on evaluating the algorithm performance using inland UAV target datasets obtained from the reference [55].

As depicted in Figure 14, this paper employs five real UAV sequences for testing, representing diverse and complex scenes. Figure 14a displays the original IR sequences used for testing, while Figure 14b–f present the results of each step in the proposed method. Figure 14g depicts the target detected after the threshold operation. Notably, Figure 14e showcases the outcome obtained through the application of the weight function, effectively filtering out most of the noise and significantly enhancing the visibility of the small target. Figure 14f represents the detection result obtained by combining RDLCM and WLCM. Finally, the threshold value is applied to filter the target region, resulting in the precise identification of the actual small target.

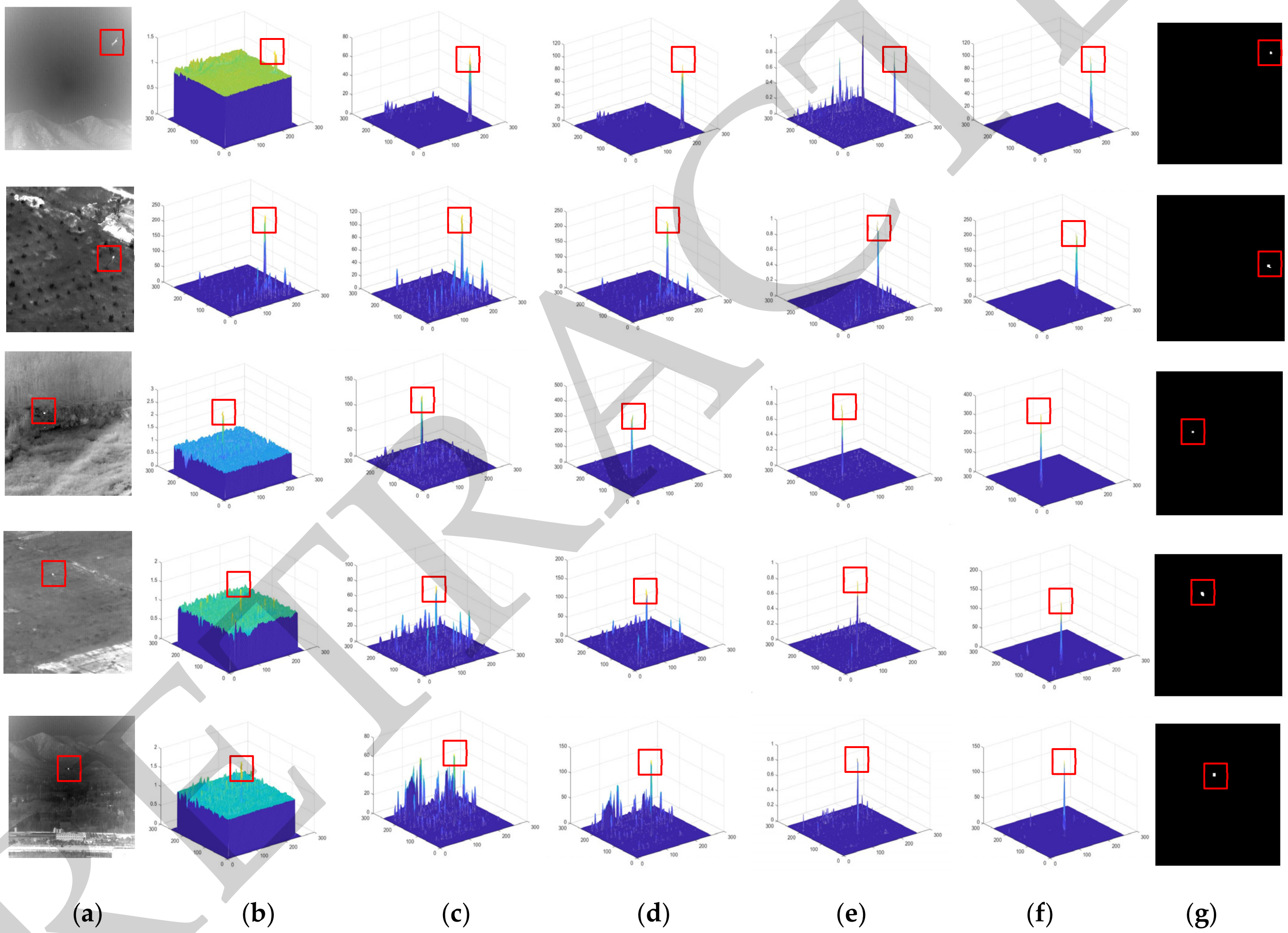

Figure 14. The 3D graphs of the results of each mechanism step for the single-frame data: (**a**) original images; (**b**) image with noise added; (**c**) result of RLCM; (**d**) result of DLCM; (**e**) result of RDLCM; (**f**) result of WLCM; (**g**) result of WRDLCM; and (**h**) final output.

Furthermore, to assess the performance of our method in the presence of noise, a certain level of noise with a mean value of 0 and a variance of 20 is added to the image in Figure 14. Figure 15 illustrates the detection results for images with added noise. As observed in Figure 15b, the image becomes considerably blurred after the introduction of random noise. However, as demonstrated in the final result depicted in Figure 15f, our algorithm exhibits robust noise resilience and maintains a satisfactory detection performance even in the presence of noise.

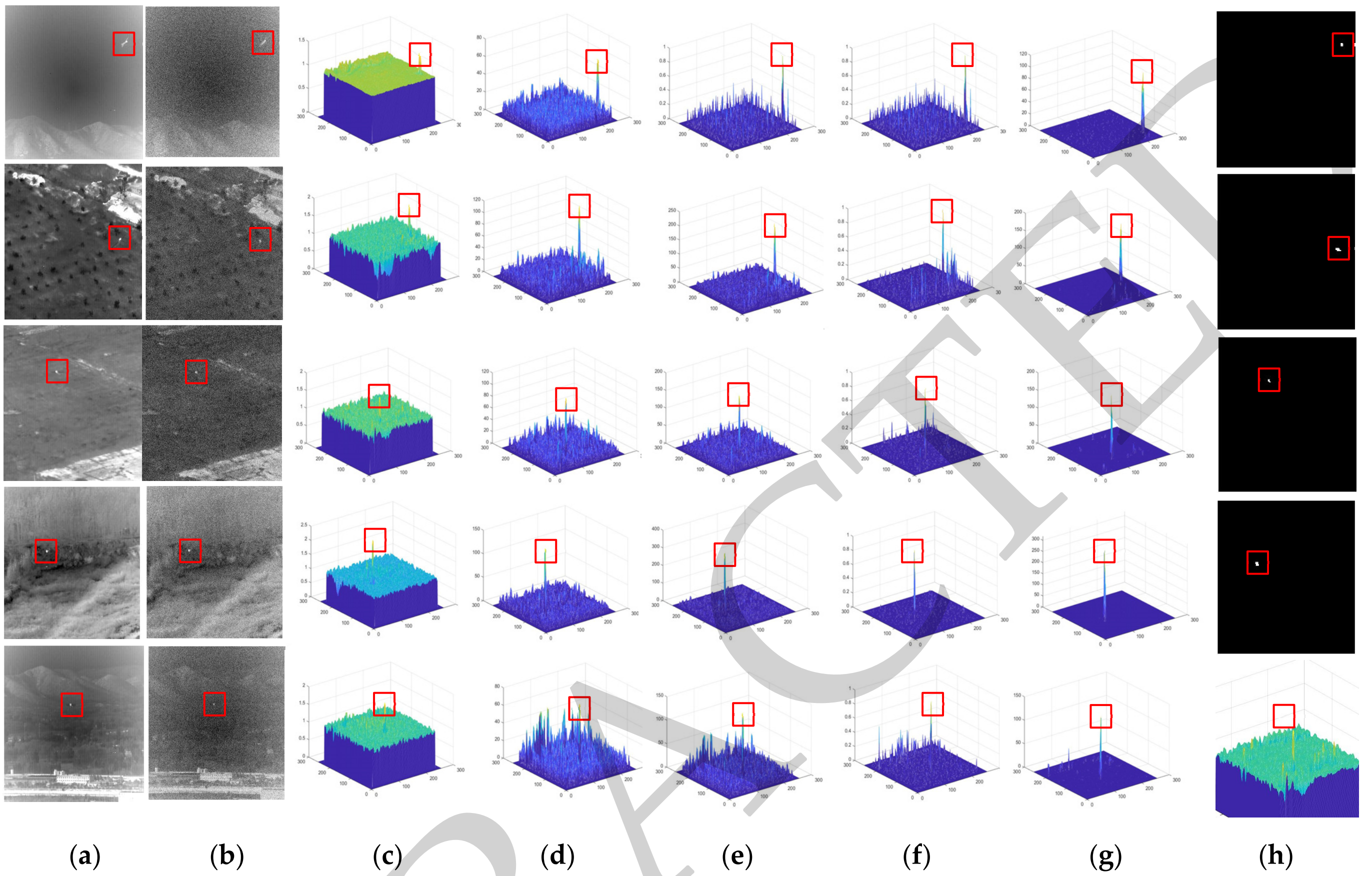

Figure 15. Stepwise 3D result diagram of the proposed method: (**a**) original images; (**b**) image with added noise; (**c**) result of RLCM; (**d**) result of DLCM; (**e**) result of RDLCM; (**f**) result of WLCM; (**g**) result of WRDLCM; and (**h**) final output.

Most of the aforementioned comparison algorithms do not consider the spatial and temporal dependencies between frames. By contrast, the method proposed in [56], referred to as MSLSTIPT, utilizes spatiotemporal information to extend image data to tensor domains. While this algorithm is novel and unique, it may not be effective for all small target detection scenarios. Figure 16 illustrates the comparison results between the MSLSTIPT algorithm and our proposed method on a small UAV target sequence, which is one of the five sequences mentioned in Figure 14. The first row shows the original images of the UAV sequence for the first six frames, while the second row presents the detection output of the MSLSTIPT algorithm. By contrast, the third row displays the detection output of our algorithm. It can be observed from the second row that the MSLSTIPT algorithm generates numerous false alarms and fails to achieve satisfactory detection performance. However, our algorithm demonstrates superior detection performance for these six sequential frames, as depicted in the third row.

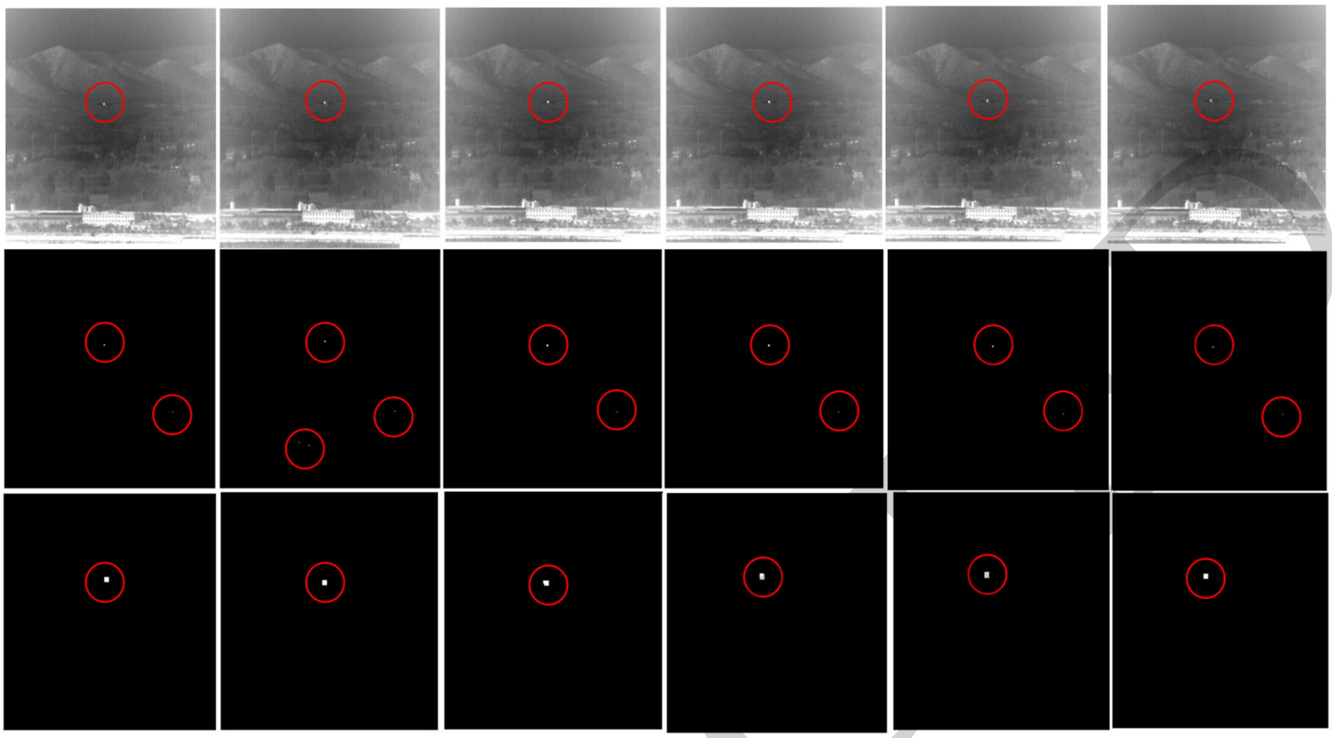

Figure 16. Target sequence and contrast detection results: (**a**–**f**) the first to sixth frames of the sequence; first row: original sequence image; second row: test results of MSLSTIPT method; third row: test results of our method.

5. Conclusions

This paper presents a novel WRDLCM algorithm that combines the RDLCM and WLCM methods. The RDLCM algorithm leverages the benefits of both ratio-type and difference-type local-contrast-based methods. It effectively suppresses various types of interference and enhances target objects without requiring any preconditioning algorithms. Additionally, a new weighting function, WLCM, is proposed. This function calculates weighting factors using mean value arithmetic operations to mitigate single random noise. By applying threshold filtering, the proposed algorithm accurately outputs the actual target. The preliminary results demonstrate the effectiveness of our target detection approach across various scenarios. Furthermore, our method is capable of detecting small targets even when their scale changes.

Moreover, our approach offers advantages in FPGA hardware processing compared to deep learning methods. While deep learning methods exhibit good detection performance, their hardware implementation is challenging and may not meet the practical requirements of industrial applications, particularly in real-world product deployment. Therefore, in future work, we aim to explore the integration of traditional algorithms with deep learning techniques to achieve real-time object detection for targets of different sizes. Additionally, we plan to focus on hardware implementation and production by leveraging FPGA technology, ensuring the wider applicability of our approach.

Author Contributions: Conceptualization, Y.C., H.W. and J.H.; methodology, Y.C. and H.W.; software, Y.C. and Y.P.; validation, Y.C., H.W. and E.M.; formal analysis, Y.C. and H.W.; writing—original draft preparation, Y.C. and H.W.; writing—review and editing, H.W., Y.P. and E.C.; supervision, E.M.; funding acquisition, Y.C., H.W. and Y.P. All authors have read and agreed to the published version of the manuscript.

Funding: This work was supported by the National Natural Science Foundation of China (grant no. U21A20447 and 61971079), the Basic Research and Frontier Exploration Project of Chongqing (grant no. cstc2019jcyjmsxmX0666), the Chongqing Technological Innovation and Application Development Project (cstc2021jscx-gksbx0051), the Innovative Group Project of the National Natural Science Foundation of Chongqing (grant no. cstc2020jcyj-cxttX0002), the Regional Creative Cooperation Program of Sichuan (grant no.2020YFQ0025), the Science and Technology Research Program of the Chongqing Municipal Education Commission (grant no. KJZD-k202000604), the Chongqing Natural Science Foundation (grant no.2022NSCQ-LZX0254), the Chongqing Technical Innovation and Application Development Special Project (grant no.CSTB2022TIAD-KPX0062),the Foundation of the Education Department of Henan Province under Grant 18B510021, and in part by the National Natural Science Foundation of China under Grant 61802455; in part by the Foundation of China Scholarship Council under Grant 202108410232; in part by the Foundation of the Science and Technology Department of Henan Province under Grant 192102210089, Grant 222102210077, and Grant 222102320370;and in part by the Foundation of the Zhoukou Science and Technology Bureau under Grant 2021GG01001; the Foundation of the Education Department of Henan Province, under grant 22B120006, the Science and Technology Research Program of the Chongqing Municipal Education Commission (grant No. KJQN202100602), a project funded by the China Postdoctoral Science Foundation (grant no. 2022MD713702), and special postdoctoral support from the Chongqing Municipal People's Social Security Bureau (grant no. 2021XM3010).

Data Availability Statement: The first six sequence data used in the experimental part of the paper cannot be shared at this time, as these data are also part of an ongoing study. However, the data are available on request from the authors. The SIRST dataset is an open single-frame dataset, and the representative images in each infrared sequence are extracted. This dataset contains 427 infrared images with a total of 480 targets. Approximately 90% of the images contain only one target, while the remaining 10% of the images feature multiple targets. Additionally, approximately 55% of the target area occupies less than 0.02% of the image. Furthermore, only 35% of the target brightness represents the highest intensity in the image. This dataset is derived from [54]. The article uses a portion of the UAV dataset, which comes from reference [55], and its collection scenarios include sky backgrounds and complex field backgrounds. It provides a set of data for one or more targets of fixed-wing UAVs through field recording and post-processing. The dataset includes a total of 22 image sequences, 30 trajectories, 16,177 frames, and 16,944 targets.

Conflicts of Interest: The authors declare no conflict of interest.

References

1. Miasnikov, E. *Threat of Terrorism Using Unmanned Aerial Vehicles: Technical Aspects*; Center for Arms Control, Energy, and Environmental Studies, Moscow Institute of Physics and Technology: Moscow, Russia, 2005.
2. Altawy, R.; Youssef, A.M. Security, privacy, and safety aspects of civilian drones: A survey. *ACM Trans. Cyber-Phys. Syst.* **2016**, *1*, 1–25. [CrossRef]
3. Kim, K. An Analysis on Anti-Drone Technology Trends of Domestic Companies Using News Crawling on the Web. *J. Adv. Navig. Technol.* **2020**, *24*, 458–464.
4. Jie, C. Research on intelligentized anti-UAV command control scheme technology. *E3S Web Conf. EDP Sci.* **2021**, *233*, 04020. [CrossRef]
5. Rawat, S.S.; Verma, S.K.; Kumar, Y. Review on recent development in infrared small target detection algorithms. *Procedia Comput. Sci.* **2020**, *167*, 2496–2505. [CrossRef]
6. Du, J.; Lu, H.; Zhang, L.; Hu, M.; Chen, S.; Deng, Y.; Shen, X.; Zhang, Y. A spatial-temporal feature-based detection framework for infrared dim small target. *IEEE Trans. Geosci. Remote Sens.* **2021**, *60*, 1–12. [CrossRef]
7. Chen, C.L.P.; Li, H.; Wei, Y.; Xia, T.; Tang, Y.Y. A local contrast method for small infrared target detection. *IEEE Trans. Geosci. Remote Sens.* **2013**, *52*, 574–581. [CrossRef]
8. Varatharasan, V.; Rao, A.S.S.; Toutounji, E.; Hong, J.-H.; Shin, H.-S. Target Detection, Tracking and Avoidance System for Low-cost UAVs using AI-Based Approaches. In Proceedings of the 2019 Workshop on Research, Education and Development of Unmanned Aerial Systems (RED UAS), Cranfield, UK, 25–27 November 2019; IEEE: New York, NY, USA, 2019; pp. 142–147.
9. Martian, A.; Chiper, F.L.; Craciunescu, R.; Vladeanu, C.; Fratu, O.; Marghescu, I. RF Based UAV Detection and Defense Systems: Survey and a Novel Solution. In Proceedings of the 2021 IEEE International Black Sea Conference on Communications and Networking (BlackSeaCom), Bucharest, Romania, 24–28 May 2021; pp. 1–4.
10. Moradi, S.; Moallem, P.; Sabahi, M.F. Fast and robust small infrared target detection using absolute directional mean difference algorithm. *Signal Process.* **2020**, *177*, 107727. [CrossRef]

11. Kwan, C.; Budavari, B. A high-performance approach to detecting small targets in long-range low-quality infrared videos. *Signal Image Video Process.* **2022**, *16*, 93–101. [CrossRef]
12. Bae, T.W.; Zhang, F.; Kweon, I.S. Edge directional 2D LMS filter for infrared small target detection. *Infrared Phys. Technol.* **2012**, *55*, 137–145. [CrossRef]
13. Kim, S. Target attribute-based false alarm rejection in small infrared target detection. *Proc. SPIE* **2012**, *8537*, 85370G. [CrossRef]
14. Deshpande, S.D.; Meng, H.E.; Ronda, V. Max-mean and max-median filters for detection of small targets. *Proc. SPIE* **1999**, *3809*, 74–83.
15. Gregoris, D.J.; Yu, S.K.; Tritchew, S.; Sevigny, L. Wavelet transform-based filtering for the enhancement of dim targets in FLIR images. *Proc. SPIE* **1994**, *2242*, 573–583. [CrossRef]
16. Bai, X.; Zhou, F. Analysis of new top-hat transformation and the application for infrared dim small target detection. *Pattern Recognit.* **2010**, *43*, 2145–2156. [CrossRef]
17. Hao, D.; Zhao, H. Adaptive method for the detection of infrared small target. *Opt. Eng.* **2015**, *54*, 113107.
18. Bi, Y.; Bai, X.; Jin, T.; Guo, S. Multiple Feature Analysis for Infrared Small Target Detection. *IEEE Geosci. Remote Sens. Lett.* **2017**, *14*, 1333–1337. [CrossRef]
19. Wang, X.; Peng, Z.; Kong, D.; Zhang, P.; He, Y. Infrared dim target detection based on total variation regularization and principal component pursuit. *Image Vis. Comput.* **2017**, *63*, 1–9. [CrossRef]
20. Shao, X.; Fan, H.; Lu, G.; Xu, J. An improved infrared dim and small target detection algorithm based on the contrast mechanism of human visual system. *Infrared Phys. Technol.* **2012**, *55*, 403–408. [CrossRef]
21. Han, J.; Ma, Y.; Zhou, B.; Fan, F.; Liang, K.; Fang, Y. A robust infrared small target detection algorithm based on human visual system. *IEEE Geosci. Remote Sens. Lett.* **2014**, *11*, 2168–2172.
22. Wang, X.; Lv, G.; Xu, L. Infrared dim target detection based on visual attention. *Infrared Phys. Technol.* **2012**, *55*, 513–521.
23. Han, J.; Liang, K.; Zhou, B.; Zhu, X.; Zhao, J.; Zhao, L. Infrared small target detection utilizing the multiscale relative local contrast measure. *IEEE Geosci. Remote Sens. Lett.* **2018**, *15*, 612–616. [CrossRef]
24. Wei, Y.; You, X.; Li, H. Multiscale patch-based contrast measure for small infrared target detection. *Pattern Recognit.* **2016**, *58*, 216–226. [CrossRef]
25. Han, J.; Liu, S.; Qin, G.; Zhao, Q.; Zhang, H.; Li, N. A Local Contrast Method Combined with Adaptive Background Estimation for Infrared Small Target Detection. *IEEE Geosci. Remote Sens. Lett.* **2019**, *16*, 1442–1446. [CrossRef]
26. Han, J.; Moradi, S.; Faramarzi, I.; Liu, C.; Zhang, H.; Zhao, Q. A Local Contrast Method for Infrared Small-Target Detection Utilizing a Tri-Layer Window. *IEEE Geosci. Remote Sens. Lett.* **2019**, *16*, 1822–1826. [CrossRef]
27. Deng, H.; Sun, X.; Liu, M.; Ye, C.; Zhou, X. Small infrared target detection based on weighted local difference measure. *IEEE Trans Geosci Remote Sens.* **2016**, *54*, 4204–4214. [CrossRef]
28. Qin, Y.; Li, B. Effective infrared small target detection utilizing a novel local contrast method. *IEEE Geosci. Remote Sens. Lett.* **2016**, *13*, 1890–1894. [CrossRef]
29. Nie, J.; Qu, S.; Wei, Y.; Zhang, L.; Deng, L. An infrared small target detection method based on multiscale local homogeneity measure. *Infrared Phys. Technol.* **2018**, *90*, 186–194. [CrossRef]
30. Chen, Y.; Song, B.; Wang, D.; Guo, L. An effective infrared small target detection method based on the human visual attention. *Infrared Phys. Technol.* **2018**, *95*, 128–135. [CrossRef]
31. Qi, H.; Mo, B.; Liu, F.; He, Y.; Liu, S. Small infrared target detection utilizing local region similarity difference map. *Infrared Phys. Technol.* **2015**, *71*, 131–139. [CrossRef]
32. Chen, Y.; Xin, Y. An efficient infrared small target detection method based on visual contrast mechanism. *IEEE Geosci. Remote Sens. Lett.* **2016**, *13*, 962–966. [CrossRef]
33. Bai, X.; Bi, Y. Derivative entropy-based contrast measure for infrared small-target detection. *IEEE Trans. Geosci. Remote Sens.* **2018**, *56*, 2452–2466. [CrossRef]
34. Nasiri, M.; Chehresa, S. Infrared small target enhancement based on variance difference. *Infrared Phys. Technol.* **2017**, *82*, 107–119. [CrossRef]
35. Gao, J.; Guo, Y.; Lin, Z.; An, W.; Li, J. Robust infrared small target detection using multiscale gray and variance difference measures. *IEEE J. Sel. Top. Appl. Earth Obs. Remote Sens.* **2018**, *11*, 5039–5052. [CrossRef]
36. Liu, J.; He, Z.; Chen, Z.; Shao, L. Tiny and dim infrared target detection based on weighted local contrast. *IEEE Geosci. Remote Sens. Lett.* **2018**, *15*, 1780–1784. [CrossRef]
37. Lv, P.; Sun, S.; Lin, C.; Liu, G. A method for weak target detection based on human visual contrast mechanism. *IEEE Geosci. Remote Sens. Lett.* **2019**, *16*, 261–265. [CrossRef]
38. Dai, Y.; Wu, Y. Reweighted infrared patch-tensor model with both nonlocal and local priors for single-frame small target detection. *IEEE J. Sel. Top. Appl. Earth Obs. Remote Sens.* **2017**, *10*, 3752–3767. [CrossRef]
39. Zhang, L.; Peng, Z. Infrared small target detection based on partial sum of the tensor nuclear norm. *Remote Sens.* **2019**, *11*, 382. [CrossRef]
40. Gupta, M.; Chan, J.; Krouss, M.; Furlich, G.; Martens, P.; Chan, M.W.; Comer, M.L.; Delp, E.J. Infrared Small Target Detection Enhancement Using a Lightweight Convolutional Neural Network. *IEEE Geosci. Remote Sens. Lett.* **2022**, *19*, 3513405. [CrossRef]
41. Dai, Y.; Wu, Y.; Zhou, F.; Barnard, K. Attentional Local Contrast Networks for Infrared Small Target Detection. *IEEE Trans. Geosci. Remote.* **2021**, *59*, 9813–9824. [CrossRef]

42. Hou, Q.; Wang, Z.; Tan, F.; Zhao, Y.; Zheng, H.; Zhang, W. RISTDNet: Robust infrared small target detection network. *IEEE Geosci. Remote Sens. Lett.* **2021**, *19*, 7000805. [CrossRef]
43. Du, J.; Lu, H.; Hu, M.; Zhang, L.; Shen, X. CNN-based infrared dim small target detection algorithm using target-oriented shallow-deep features and effective small anchor. *IET. Image Process.* **2021**, *15*, 1–15. [CrossRef]
44. Miezianko, R. Terravic Research Infrared Database. IEEE OTCBVS WS Series Bench. Available online: http://vcipl-okstate.org/pbvs/bench/index.html (accessed on 30 January 2020).
45. Cui, Z.; Yang, J.; Jiang, S.; Li, J. An infrared small target detection algorithm based on high-speed local contrast method. *Infrared Phys. Technol.* **2016**, *76*, 474–481. [CrossRef]
46. Xia, C.; Li, X.; Zhao, L.; Xia, C.; Shu, R. Infrared small target detection based on multiscale local contrast measure using local energy factor. *IEEE Geosci. Remote Sens. Lett.* **2019**, *17*, 157–161. [CrossRef]
47. Khaledian, P.; Moradi, S.; Khaledian, E. A new method for detecting variable-size infrared targets. In Proceedings of the Sixth International Conference on Digital Image Processing (ICDIP 2014), SPIE, Athens, Greece, 5–6 April 2014; Volume 9159, pp. 299–304.
48. Zhang, W.; Cong, M.; Wang, L. Algorithms for optical weak small targets detection and tracking: Review. In Proceedings of the 2003 IEEE International Conference on Neural Networks and Signal Processing, Nanjing, China, 14–17 December 2003; Volume 1, pp. 643–647. [CrossRef]
49. Wang, L.; Li, Z.; Deng, X. An infrared small target detection method based on visual spatio-temporal local contrast measure. *Proc. SPIE* **2017**, *10255*, 102552Z. [CrossRef]
50. Sun, S.G.; Kim, K.T.; Kim, S. Highly efficient supersonic small infrared target detection using temporal contrast filter. *Electronics Letters.* **2014**, *50*, 81–83.
51. Deng, L.; Zhu, H.; Tao, C.; Wei, Y. Infrared moving point target detection based on spatial-temporal filter. *Infrared Phys. Technol.* **2016**, *76*, 168–173. [CrossRef]
52. Han, J.; Liu, C.; Liu, Y.; Luo, Z.; Zhang, X.; Niu, Q. Infrared Small Target Detection Utilizing the Enhanced Closest-Mean Background Estimation. *IEEE J. STARS* **2021**, *14*, 645–662. [CrossRef]
53. Han, J.; Moradi, S.; Faramarzi, I.; Zhang, H.; Zhao, Q.; Zhang, X.; Li, N. Infrared small target detection based on the weighted strengthened local contrast measure. *IEEE Geosci. Remote Sens. Lett.* **2021**, *18*, 1670–1674. [CrossRef]
54. Dai, Y.; Wu, Y.; Zhou, F.; Barnard, K. Asymmetric contextual modulation for infrared small target detection. In Proceedings of the IEEE/CVF Winter Conference on Applications of Computer Vision, Waikoloa, HI, USA, 3–8 January 2021; pp. 950–959.
55. Hui, B.; Song, Z.; Fan, H.; Zhong, P.; Hu, W.; Zhang, X.; Lin, J.; Su, H.; Jin, W.; Zhang, Y.; et al. Infrared dim and small aircraft target detection and tracking dataset from infrared image in ground/air background. *Chin. Sci. Data* **2020**, *5*, 286–297.
56. Sun, Y.; Yang, J.; An, W. Infrared Dim and Small Target Detection via Multiple Subspace Learning and Spatial-Temporal Patch-Tensor Model. *IEEE Trans. Geosci. Remote Sens.* **2021**, *59*, 5. [CrossRef]